

Conversion of Potassium Titanate Nanowires into Titanium Oxynitride Nanotubes

Yen-Ju Wei,[†] Chih-Wei Peng,[†] Ta-Ming Cheng,[†] Huang-Kai Lin,[†] Yu-Liang Chen,[†] Chi-Young Lee,[‡] and Hsin-Tien Chiu^{*,†}

[†]Department of Applied Chemistry, National Chiao Tung University, Hsinchu, Taiwan 30050, R. O. C.

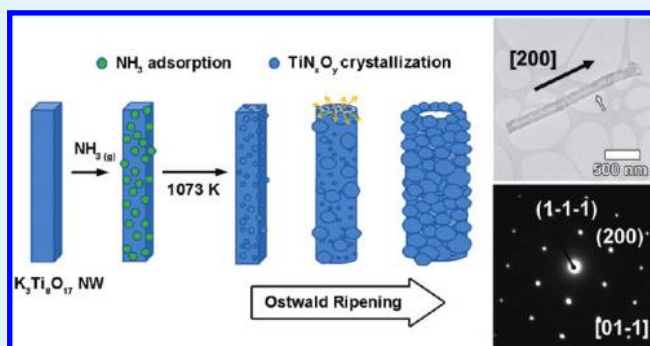
[‡]Department of Materials Science and Engineering and Center for Nanotechnology, Materials Science, and Microsystems, National Tsing Hua University, Hsinchu, Taiwan 30043, R. O. C.

S Supporting Information

ABSTRACT: Tunnel-structured potassium titanate with a $K_3Ti_8O_{17}$ phase was synthesized by direct oxidation of titanium powder mixed with $KF(aq)$ in water vapor at 923 K. The reaction conditions were adjusted so that uniform single crystalline potassium titanate nanowires with $[010]$ growth direction (length: 5–30 μm , diameter: 80–100 nm) were obtained. Nitridation of the nanowires by $NH_3(g)$ at 973–1073 K converted the titanate nanowires into rock-salt structured cubic phase single crystalline titanium oxynitride TiN_xO_y nanotubes ($x = 0.88, y = 0.12$, length = 1–10 μm , diameter = 150–250 nm, wall thickness = 30–50 nm) and nanorods ($x = 0.5, y = 0.5$, length = 1–5 μm , diameter = 100–200 nm) with rough surfaces and $[200]$ growth direction. The overall conversion of the titanate nanowires into the nanotubes and the nanorods can be rationalized by Ostwald ripening mechanism. We fabricated an electrode by adhering TiN_xO_y nanotubes (0.2 mg) on a screen-printed carbon electrode (geometric area: 0.2 cm^2). Electrochemical impedance spectroscopy demonstrated its charge transfer resistance to be 20 Ω . The electrochemical surface area of the nanotubes on the electrode was characterized by cyclic voltammetry to be 0.32 cm^2 . This property suggests that the TiN_xO_y nanostructures can be employed as potential electrode materials for electrochemical applications.

The overall conversion of the titanate nanowires into the nanotubes and the nanorods can be rationalized by Ostwald ripening mechanism. We fabricated an electrode by adhering TiN_xO_y nanotubes (0.2 mg) on a screen-printed carbon electrode (geometric area: 0.2 cm^2). Electrochemical impedance spectroscopy demonstrated its charge transfer resistance to be 20 Ω . The electrochemical surface area of the nanotubes on the electrode was characterized by cyclic voltammetry to be 0.32 cm^2 . This property suggests that the TiN_xO_y nanostructures can be employed as potential electrode materials for electrochemical applications.

KEYWORDS: potassium titanate, titanium oxynitride, nanowire, nanotube



INTRODUCTION

Titanium nitride, TiN, is frequently employed as a coating material because of its extreme hardness, low electrical resistivity, high chemical stability, and golden color.¹ Typical applications of TiN films include protective and decorative coatings on cutting tools and diffusion barriers in integrated circuit devices.^{2,3} When some N atoms in TiN are replaced by O atoms, titanium oxynitride, TiN_xO_y , can be produced.^{4,5} In addition to the applications described above, TiN_xO_y is a more attractive material than TiN because the properties of the oxynitride can be tuned as a function of its N/O ratio in principle. Recently, applications of nanostructured TiN as electrodes for super capacitors and dye-sensitized solar cells (DSSCs) have been reported.^{6–9} In addition, similarities between the electronic structure of metal nitrides and that of noble metals may lead to comparable electrocatalytic activities.^{7–9} Thus, due to the high electrical conductivity and low material cost, it is suggested that both TiN and TiN_xO_y are potential substitutes for noble metals. Conversions of metal oxides into nitrides and oxynitrides were realized by reacting oxides and their precursors with NH_3 , amine, amide, azide and urea.^{1,10–14} Though the synthetic approaches varied widely, there were limited number of researches about the syntheses

of nanosized metal nitrides and oxynitrides, especially in one-dimensional (1D) form.^{13–16} Only one article reported the fabrication of 1D titanium oxynitride.¹⁴

Here we report a large-scale synthesis potassium titanate nanowires (PT-NWs) as the precursor material via a modified literature route.¹⁷ Then, we react PT-NWs further in $NH_3(g)$ at high temperatures to convert them into cubic phase titanium oxynitride (TON) in the forms of highly crystalline nanorod (NR) and rodlike nanotube (RNT) for the first time in literature. The overall reaction steps are summarized in Scheme 1. In addition, we discover that the oxynitride can be used as a potential electrode material for electrochemistry applications. Our findings are discussed below.

EXPERIMENTAL SECTION

All reactions were performed in a horizontal atmospheric pressure hot-wall quartz tube reactor heated by a tube furnace. Figures S1 and S2 in the Supporting Information showed the experimental setups for the

Received: September 8, 2010

Accepted: September 22, 2011

Published: September 22, 2011

Scheme 1. Overall rReactions

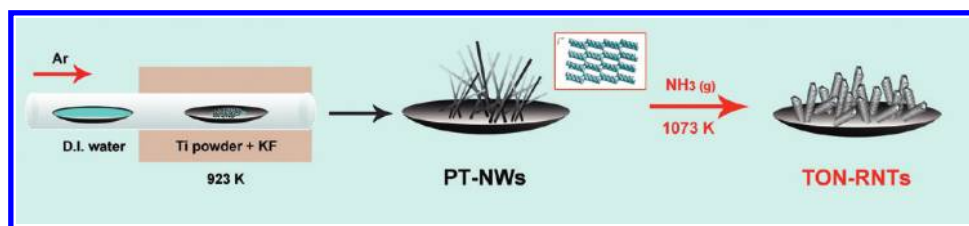


Table 1. Summary of Products

sample	preparation	color and morphology	diameter (nm)	length (μm)	phase	estimated composition	specific surface area (m^2/g)
PT-NW	Ti(s)/KF(aq) (1:3) ^a , in H ₂ O(g), 923 K, 24 h	white, nanowires	80–100	5–30	K ₃ Ti ₈ O ₁₇	KTi _{2.5} O _{5.9} ^c	3.3
TON-RNT-A	PT-NWs, in NH ₃ (g) 20 sccm, 1073 K, 10 h	black, rodlike nanotubes	150–250	1–5	TiN/TiO ^b	TiN _{0.98} O _{0.44} ^d	19.6
TON-RNT-B	PT-NWs, in NH ₃ (g) 50 sccm, 1073 K, 10 h	black, rodlike nanotubes	150–250	1–10	TiN/TiO ^b	TiN _{0.92} O _{0.31} ^d	22.4
TON-NR	PT-NWs in NH ₃ (g) 20 sccm, 973 K, 10 h	black, nanorods	100–200	1–5	TiN/TiO ^b	TiN _{0.62} O _{1.43} ^d	15.5

^a Molar ratio. ^b TiN and TiO are isostructural. ^c Determined from the corresponding EDX data in the Supporting Information. ^d Calculated from the corresponding EA and TGA data, see Table S8 in the Supporting Information.

preparations of PT-NWs and TON nanomaterials, respectively. The essential products are summarized in Table 1.

Preparation of PT-NWs. Ti powders (0.1 g, 2 mmol, Aldrich, 99.7%) were mixed with KF(aq) (10.9 M, 0.575 mL, Riedel-de Haën) with a mole ratio of 1:3. After being ultrasonicated for 5 min, the mixture was transferred to a 4 cm-quartz boat and placed at center of the heating zone in the reactor. Since KF etched the boat, a new boat was used for every reaction. Another quartz boat filled with deionized water (10 mL) was placed at an upstream position 30 cm away from the center. As the mixture was heated at 923 K, Ar (5 sccm) was allowed to flow through the reactor for 24 h. The material was washed with deionized water, centrifuged, and dried in air to offer a white powder. A summary of the results of other reaction conditions was listed in Table S1 in the Supporting Information.

Preparation of TON Nanostructures. In a typical experiment, PT-NWs (0.15 g) were heated at 1073 K (ramping rate: 5 K min⁻¹) for 10 h in the nitridation reactor (NH₃(g), flow rate: 20 sccm, Sanying, 99.9%) shown in Figure S2 in the Supporting Information. After the reaction, the product was rinsed with deionized water and dried in air to give a black powder of TON-RNT-A. Other TON products, TON-RNT-B and TON-NR, are listed in Table 1. A summary of the results from other attempted reaction conditions was shown in Table S2 in the Supporting Information.

Instruments for Characterizations. Scanning electron microscopic (SEM) images were obtained using a JEOL JSM-7401F at 15 kV. X-ray diffraction (XRD) patterns were collected using a BRUKER AXS D8 ADVANCE, a Bragg–Brentano-type diffractometer with Cu K α 1 radiation. A software, Celref, was employed to evaluate their lattice parameters by refining the corresponding XRD patterns. Transmission electron microscopic (TEM) studies were carried out on a JEOL JEM-2010 at 200 kV. X-ray photoelectron spectroscopic (XPS) measurements were performed on a Perkin PHI-1600 photoelectron spectrometer using monochromatic Al K α radiation (photon energy 1486.6 eV). Nitrogen contents were obtained using HERAEUS CHN-O-RAPID elemental analyzer (EA), carried out in oxygen at 1223 K. Thermogravimetric analyses (TGA) were conducted to estimate the Ti contents in the samples. Brunauer–Emmett–Teller (BET) surface area measurements were performed on a Micrometrics ASAP 2020. The powders were degassed at 353 K 1320 Pa for 18 h prior to the analyses.

Electrochemical Measurements. Electrochemical impedance spectroscopic (EIS) and electrochemical surface area (ESA) measurements were carried out using a potentiostat (CHI 6081C) equipped with three electrodes. The working electrode was fabricated by using TON-RNT-A. A powder of TON-RNT-A (0.2 mg), dispersed in ethanol (20 μL) and ultrasonicated for 5 min, was dropped on a screen-printed carbon (SPC) electrode (Zensor, diameter: 5 mm). The as-fabricated electrode was designated TON-RNT-A/SPC. The counter electrode was a Pt wire. An Ag/AgCl electrode was used as the reference electrode, with a potential of 0.2 V vs the standard hydrogen electrode (SHE). For EIS studies, K₃Fe(CN)₆(aq) was prepared in a PBS (pH 7.4, 0.01 M, 10 mL) solution as the supporting electrolyte. Both TON-RNT-A/SPC and a commercial flat Au electrode were used as the working electrodes for comparison. The initial potential was set at 0.22 V and the frequency range was from 1 \times 10⁵ to 1 Hz with an AC amplitude 5 mV. The experimental data were fitted with the software of CHI 6081C. For cyclic voltammetric (CV) studies, TON-RNT-A/SPC was studied in an aqueous solution containing K₃Fe(CN)₆ (2 mM) and KNO₃ (1M).

RESULTS AND DISCUSSION

Preparation and Characterization of Potassium Titanate Nanowires. We modified a literature route to synthesize PT-NWs. In the previous study, long PT-NWs were fabricated on Ti foils and thin films.¹⁷ In this paper, we synthesized PT-NWs in a similar way. In order to grow phase-pure PT-NWs, several growth conditions were adjusted. Instead of Ti foils, we used Ti powder as the Ti source. The powder was mixed with KF(aq) and reacted with H₂O(g) at high temperatures inside a hot-wall reactor. Several reaction conditions, as summarized in Table S1 in the Supporting Information, were attempted. Phase-pure white PT-NWs were obtained in the reaction started with an initial Ti/KF molar ratio of 1:3 and reacted at 923 K for 24 h. Characterizations of PT-NWs will be discussed below. Some of the results of PT-NWs are summarized in Table 1.

As shown in Figure 1a, a low magnification SEM image displays a high density of NWs with several micrometers in length. The EDX (inset) indicates that the NWs are composed of K, Ti and O. As shown in Figure 1b, the NWs are estimated to be

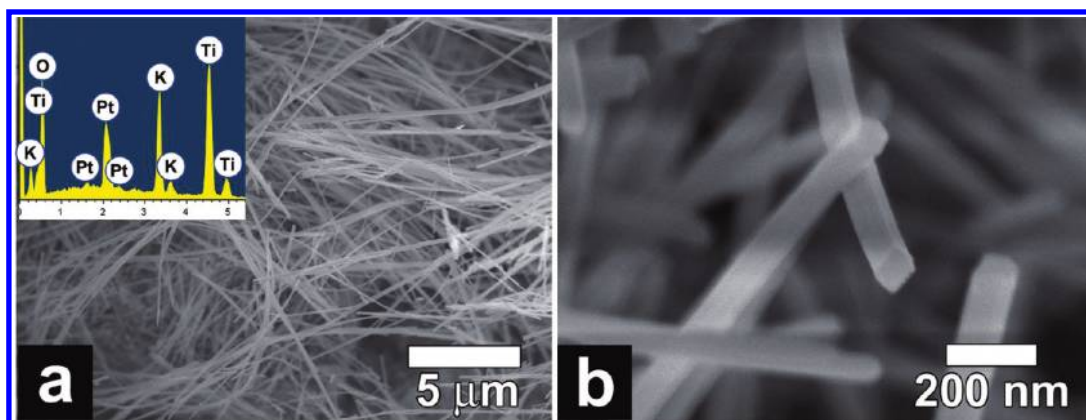


Figure 1. (a) Low-magnification SEM image (inset, EDX; to increase conductivity, a layer of Pt was sputtered on the sample) and (b) high-magnification SEM image of PT-NWs.

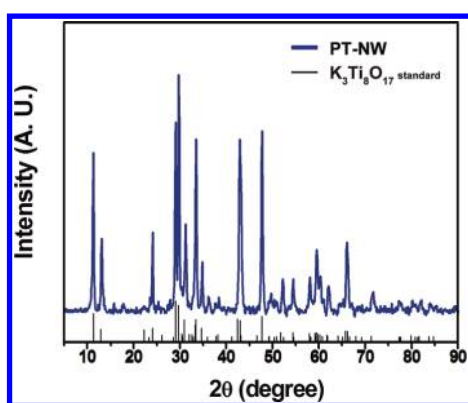


Figure 2. XRD pattern of PT-NWs. The standard pattern of $K_3Ti_8O_{17}$ (JCPDS 72–1699) is shown for comparison.

80–100 nm in diameters. The end of each NW tip appears to be rectangular. The XRD pattern of PT-NWs, shown in Figure 2, matches the pattern of the tunnel-structured potassium titanate $K_3Ti_8O_{17}$ (JCPDS 72–1699) well. The peak observed at $2\theta = 11.32^\circ$ is assigned to be reflection from $K_3Ti_8O_{17}$ (200) planes. The detailed database assignments were listed in Table S3 in the Supporting Information. TEM studies of an as-grown PT-NW are shown in Figure 3. The low magnification image (Figure 3a) shows a NW with a length of ca. $6\ \mu\text{m}$. The EDX (inset) indicates that the NW contains K, Ti, and O. The Ti/K ratio ranges from 2.3 to 2.8 throughout the NW, as shown in the semiquantitative EDX data listed in Table S4 in the Supporting Information. They are close to the theoretical Ti/K value of $K_3Ti_8O_{17}$, 2.67. The enlarged view of the NW tip is shown in Figure 3b. It displays that the NW is ca. 90 nm in diameter. The selected area electron diffraction (SAED) pattern shown in Figure 3c, taken from the tip of the NW, suggests that the sample is single crystalline. The observed spots are determined to be from (200) and (1–10) planes of monoclinic $K_3Ti_8O_{17}$ with [001] zone axis. Figure 3d exhibits the HRTEM image from the squared region in Figure 3b. The estimated lattice spacings 0.38 and 0.80 nm are assigned to (200) and (1–10) planes, respectively. On the basis of the results from the XRD and the TEM studies, the NWs are determined to be single crystalline $K_3Ti_8O_{17}$ growing along the [010] direction. Figure 3e shows the polyhedral representation of the crystal structure for $K_3Ti_8O_{17}$, projected along the c axis. It is worthwhile

to note that although we employed a modified literature procedure to prepare PT-NWs, the NWs synthesized in the original report were characterized to be $K_2Ti_8O_{17}$.¹⁸ We attribute the difference to the variations in the synthetic procedures.

The growth of PT-NWs was highly dependent on the reaction conditions. As listed in Table S1 in the Supporting Information, when less KF was used, another type of potassium titanate, with the hollandite structure ($K_{1.28}Ti_8O_{16}$, JCPDS 84–2058), was also obtained as block-like particles in the products. The characterizations, including XRD, TEM, ED, and EDX, were summarized in Figures S3 and S4 and Table S5 in the Supporting Information. The EDX data suggested that the hollandite obtained was slightly K deficient. We discovered that the hollandite formation was suppressed when a low Ti/K ratio of 1/3 and an extended reaction time were employed. These might cause more K^+ ions to diffuse into the titanate structures to form more tunnel structured $K_3Ti_8O_{17}$ NWs at 923 K.

In addition, we also confirmed that that PT-NWs only grew favorably when KF(aq) was mixed with Ti(s). When other salts, such as KCl, KBr, KOH, and NaF, were used, few NWs were formed, as shown in Figure S5 in the Supporting Information. These observations paralleled the studies reported previously.¹⁷ We suggest that F^- ions probably etched the Ti surface more effectively than the other anions. The as-formed surface Ti–F underwent facile exchange with H_2O to form surface Ti–OH species.¹⁸ Then, depending on the reaction conditions, the K^+ ions stabilized the Ti–OH species and induced the growths of the titanates observed.

Preparation and Characterization of Titanium Oxynitride Nanostructures. The PT-NWs described above were heated in $NH_3(g)$ to produce black titanium oxynitride nanostructures: TON-RNT-A, TON-RNT-B, and TON-NR. A summary of experimental conditions and morphological properties are listed in Table 1. Other attempted reactions were summarized in Table S2 in the Supporting Information. Their SEM and XRD data were shown in Figure S7 in the Supporting Information.

SEM images in Figure 4 show the morphologies of TON-RNT-A and TON-RNT-B produced by the nitridation of PT-NWs at 1073 K for 10 h in $NH_3(g)$ flow rates 20 and 50 sccm, respectively. In Figure 4a, the low magnification image displays that the lengths of the 1D TON-RNT-A nanostructures are 1–5 μm , clearly much shorter than the data of their precursors. The EDX (inset) shows that TON-RNT-A contains Ti, N, and O

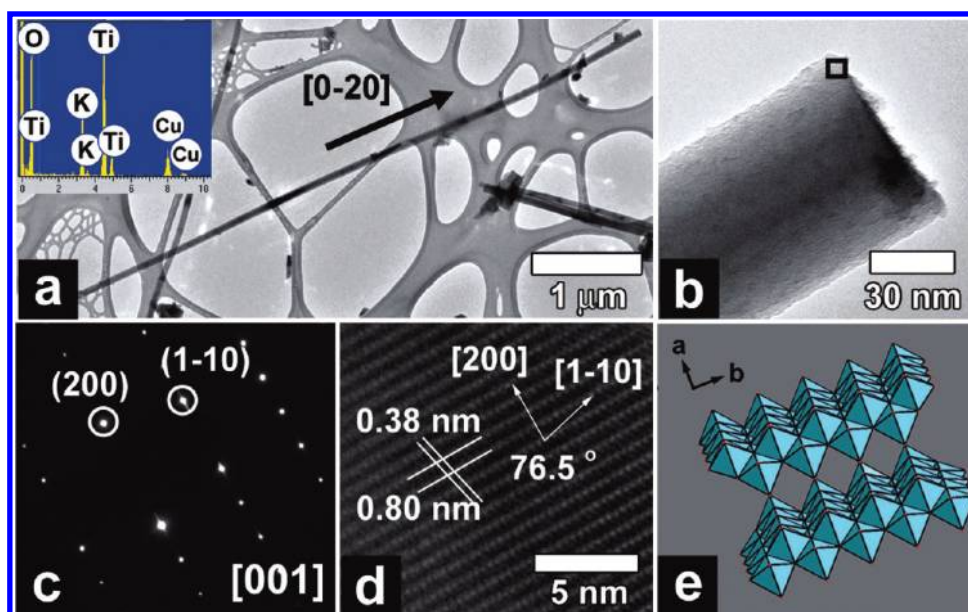


Figure 3. TEM studies of an isolated PT-NW. (a) Low-magnification image (Inset, EDX; the signals of Cu were from the copper grid), (b) high-magnification image, (c) SAED pattern, (d) HRTEM image of the squared area in b, and (e) polyhedral representation of the crystal structure for $K_3Ti_8O_{17}$, projected along the c axis.

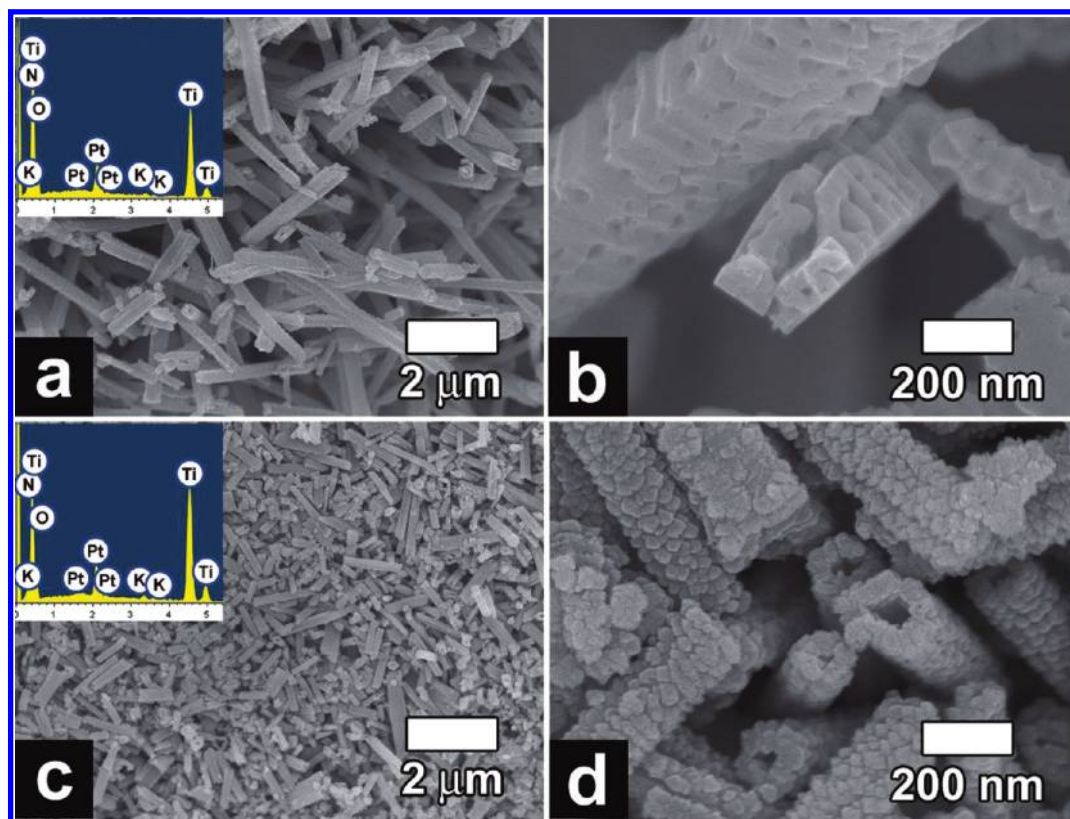


Figure 4. Low- and high-magnification SEM images of (a, b) TON-RNT-A and (c, d) TON-RNT-B (insets of a and c, EDX data; to increase conductivity, a layer of Pt was sputtered on the sample).

atoms majorly. Only a trace of K signals can still be observed. The high-magnification image shown in Figure 4b reveals the tube-like open ended tip of a TON-RNT-A. The diameter of TON-RNT-A is much wider than that of the original NW. The

rectangular NTs have an outer diameter 150–500 nm and an inner diameter 80–400 nm. The NT surface is much more rough and porous than the original appearance of the NW. As the flow rate of $NH_3(g)$ for nitridation was increased to 50 sccm,

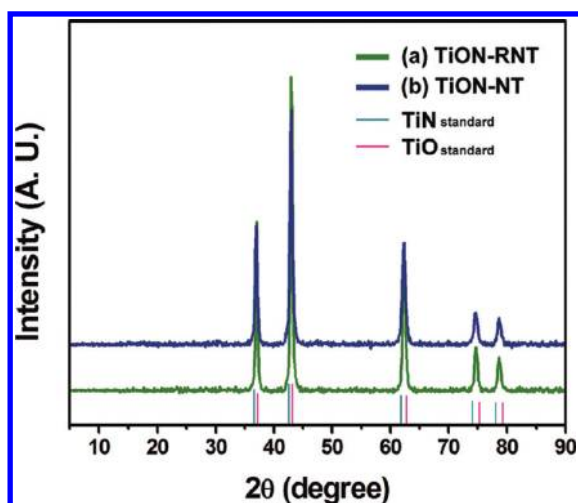


Figure 5. XRD patterns of (a) TON-RNT-A and (b) TON-RNT-B. For comparisons, TiN (JCPDS 38–1420) and TiO (JCPDS 77–2170) standards are shown.

TON-RNT-B was produced. As shown in Figure 4c, the sample contains short 1D segments with lengths less than $2\ \mu\text{m}$. It is also composed of Ti, N, and O as the main constituents. As displayed in Figure 4d, the surface of TON-RNT-B appears to be rougher but less porous than those of TON-RNT-A. In addition, the NTs in TON-RNT-B are round in shape instead of rectangular. The NTs in TON-RNT-B have outer and inner diameters similar to the values of TON-RNT-A. But unlike the tube wall of TON-RNT-A, which appears to be composed of fused nanoblocks, the wall of TON-RNT-B shows a structure of aggregated nanoparticles with 20–50 nm in size. The nitridation of the NWs not only shortened the lengths and widened the diameters but also changed the structures to NTs with obvious increase of the specific areas (Table 1). The XRD patterns of TON-RNT-A and TON-RNT-B are shown in Figure 5. Both of them display five diffraction peaks at $2\theta = 36.98, 42.97, 62.30, 74.65,$ and 78.60° . Each of them is at a position between the corresponding peaks of cubic TiN (JCPDS 38–1420) and cubic TiO (JCPDS 77–2170), two structure with very similar lattice parameters (see Table S6 in the Supporting Information). A series of samples with different nitridation time were examined by XRD also. The refinements confirmed the products were rock-salt structured cubic phase crystals (see Table S7 in the Supporting Information). When the nitridation time was performed for 5 h, both the lattice parameter and the crystal volume were close to those of TiO. As the nitridation time was extended, these values increased as well. After nitridation for 24 h, the sample showed a lattice parameter close to that of TiN. Presumably, extended nitridation replaced more O atoms with smaller atomic radius by larger N atoms, causing the lattice parameters to increase. The nitrogen contents, obtained from the EA studies, of TON-RNT-A, TON-RNT-B and TON-NR were listed in Table S8 in the Supporting Information. The quantities of Ti in the sample were estimated from the TGA results. In TGA analyses, we heated TON-RNT-A, TON-RNT-B, and TON-NR under air and raised the temperature to 1273 K. The TGA data were shown in Figure S6 in the Supporting Information. Obvious weight increases were observed above 623 K. Through XRD studies, we found that the powders were converted to TiO_2 . The Ti contents were evaluated accordingly and listed in Table S8 in the Supporting

Information. Furthermore, we could approximate the original O in the original samples by subtracting the Ti and N concentrations obtained from the TGA and the EA results. The chemical compositions of these compounds are listed in Table 1. For TON-RNT-A, TON-RNT-B, and TON-NR, their formulas are determined to be $\text{Ti}_{0.98}\text{O}_{0.44}$, $\text{Ti}_{0.92}\text{O}_{0.31}$, and $\text{Ti}_{0.62}\text{O}_{1.43}$, respectively.

The NTs were further analyzed using TEM. In Figure 6a, a low-magnification image shows a NT isolated from TON-RNT-A. The sample is $2.2\ \mu\text{m}$ in length, 150 nm in outer diameter, and 80 nm in inner diameter. The high magnification image in Figure 6b displays the rough and porous surface of TON-RNT-A. This is in good agreement with the SEM observations. The SAED pattern in Figure 6c, taken from the area pointed by the white arrow in Figure 6a, suggests that the NT is single crystalline although the sample is rough and porous. The observed spots are determined to be from (200) and (1–1–1) planes of a cubic phase solid with [01–1] zone axis. The lattice parameter a , estimated from the pattern, is 0.421 nm, close to the standard values of cubic TiN (JCPDS 38–1420) and cubic TiO (JCPDS 77–2170), 0.424 and 0.418 nm, respectively. Figure 6d displays a low-magnification TEM image of a NT isolated from TON-RNT-B. The sample is $5\ \mu\text{m}$ long, 380 nm wide outside the NT, 280 nm wide inside the NT. The further enlarged image in Figure 6e displays the body of the TON-RNT-B from the area pointed by the white arrow. For TON-RNT-B, the rough surface of the NT agrees with the SEM observations shown in Figure 4. The SAED pattern (Figure 6f), with [001] zone axis, reveals slightly diffused spots. These are assigned to (200) and (020) planes perpendicular to each other. The lattice parameter a is estimated to be 0.422 nm. This value is close to the standard values of cubic TiN and cubic TiO also. On the basis of the results from the XRD and the TEM studies, we conclude that both TON-RNT-A and TON-RNT-B are highly ordered cubic phase titanium oxynitrides with preferred [200] orientations.

To evaluate the chemical environment of the elements in the NT, we carried out XPS studies. The high resolution spectra in Figure 7a show the signals assigned to Ti_{2p} electrons. The as-received sample shows two major peaks at 459.0 and 464.6 eV. These are assigned to Ti $2p_{3/2}$ and Ti $2p_{1/2}$ electrons, respectively, in the Ti(IV)–O environment.¹⁹ After the surface was sputtered by Ar^+ ions (120 s), the signals at 455.1 and 461.2 eV become the main peaks. They are assigned to Ti $2p_{3/2}$ and Ti $2p_{1/2}$ electrons, respectively, in a less oxidized environment.¹⁹ In Ti(II)–O and Ti–N solids, the Ti $2p_{3/2}$ electrons were observed at 455.1 and 455.2 eV, respectively. In Figure 7b, the peak at 397.3 eV is assigned to the N 1s atoms in a Ti–N solid.¹⁹ After the Ar^+ sputtering, the N 1s intensity is increased. This suggests that after the sputtering step, more nitrogen containing material underneath the surface layers is exposed. In addition, the signals seen at 293.8 and 296.6 eV are assigned to K $2p_{3/2}$ and K $2p_{1/2}$ electrons of potassium ions on the surface, as shown in Figure 7c. They decrease significantly after the Ar^+ sputtering. This suggests that after the nitridation of PT-NWs, most potassium ions shifted from the structure inside to the surface. In Figure 7d, the signal at 531.1 eV is assigned to O 1s electrons. Because the value is higher than that of O 1s electrons in Ti(IV)–O solids, 530.0 eV, we suggest that the O atoms are bounded to Ti atoms in lower oxidation states, such as Ti(II).¹⁹ The O 1s signal is reduced after the sputtering. The XPS survey scan of the as-prepared TON-RNT-A was shown in Figure S8 in the Supporting Information. It displayed the presence of K, Ti, O, N, and C atoms on the surface.

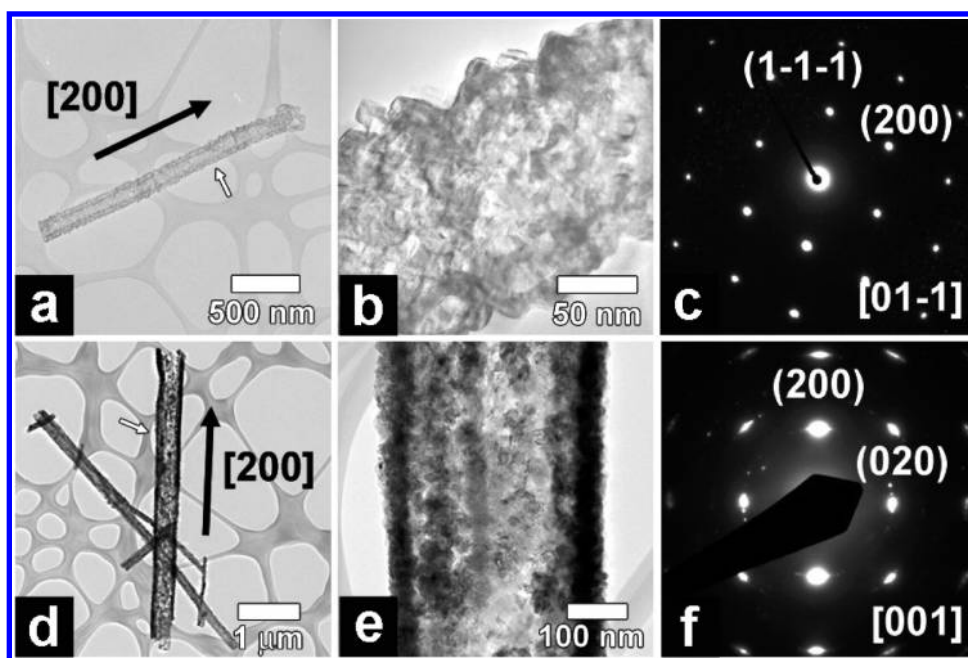


Figure 6. TEM studies of NTs. (a) Low-magnification image, (b) high-magnification image of the area pointed by the white arrow in a, and (c) SAED of TON-RNT-A. (d) Low-magnification image, (e) high-magnification image of the area pointed by the white arrow in d, and (f) SAED of TON-RNT-B.

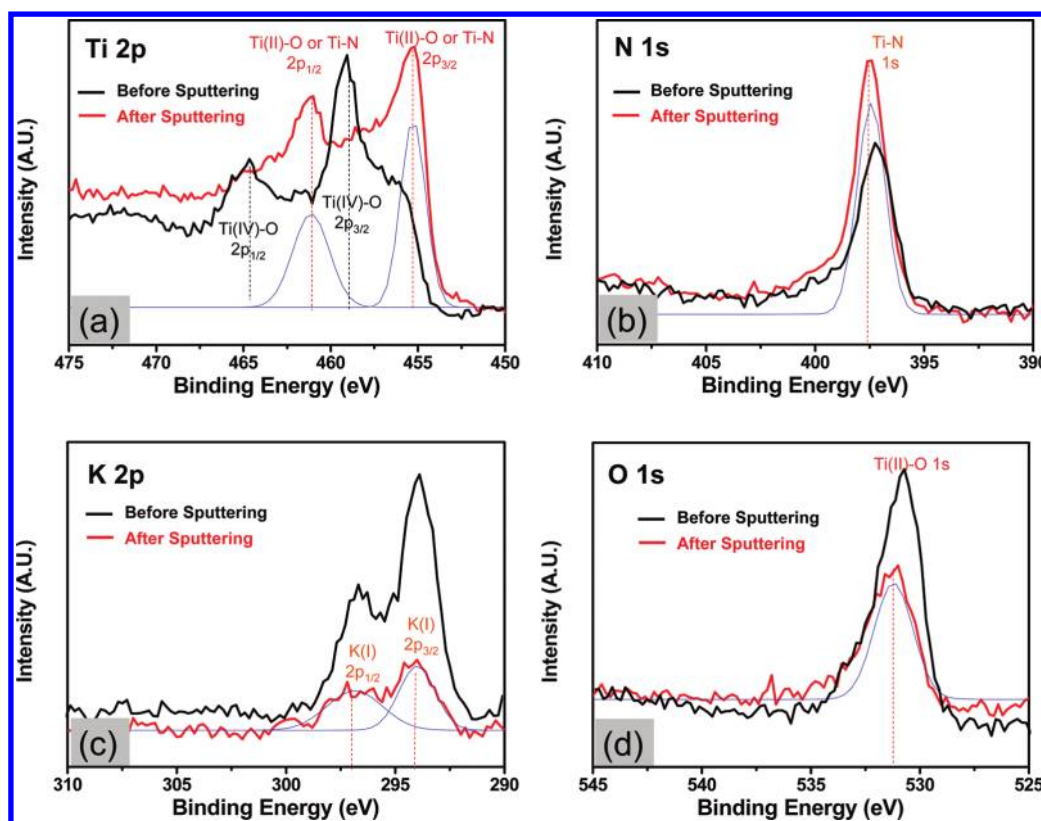


Figure 7. High-resolution XPS spectra of TON-RNT-A. (a) Ti 2p, (b) N 1s, (c) K 2p, and (d) O 1s electrons. (Red lines are signals obtained after Ar^+ sputtering for 120 s. Blue lines are the curves fitted for the spectra obtained after sputtering.)

The C 1s signal diminished significantly after the Ar^+ sputtering. We assign the origin of the signal to adventitious carbon on the surface.

Proposed TiN_xO_y Nanotube Growth Pathway. To rationalize how the TiN_xO_y NTs are formed, a pathway is proposed in Scheme 2. In the first step, $\text{NH}_3(\text{g})$ molecules adsorb on the

Scheme 2. Proposed TON-RNT Growth Pathway

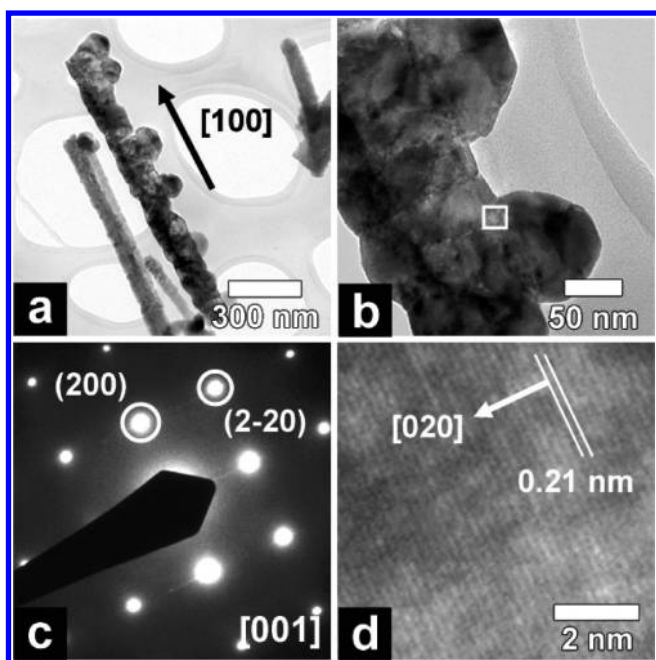
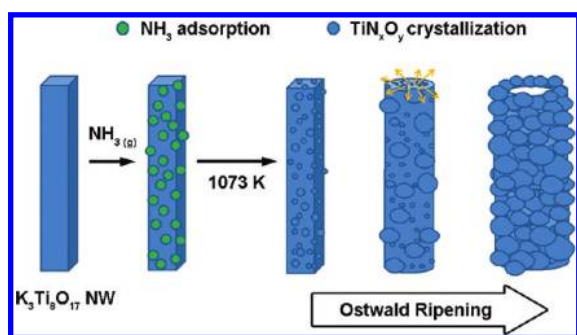


Figure 8. TEM studies of TON-NR. (a) Low- and (b) high-magnification image. (c) SAED and (d) HRTEM image of the squared area in b.

PT-NW surface and diffuse into the NW through the vacancies in the structure. Although the decomposition of $\text{NH}_3(\text{g})$ to $\text{N}_2(\text{g})$ and $\text{H}_2(\text{g})$ is kinetically slow in gas phase,²⁰ the adsorbed $\text{NH}_{3(\text{ads})}$ starts to dissociate on the surface into $\text{NH}_x(\text{ads})$ and $\text{H}(\text{ads})$ fragments at temperatures above 573 K.^{21,22} The dehydrogenation rate increases with the rise of temperature. Whereas some $\text{H}(\text{ads})$ atoms recombine and desorb from the surface as $\text{H}_2(\text{g})$, other $\text{H}(\text{ads})$ atoms combine with O atoms in the PT-NW to produce $\text{OH}(\text{ads})$ and $\text{H}_2\text{O}(\text{ads})$. Eventually, active N(ads) atoms are formed.^{23,24} They can substitute O atoms and form bonds to Ti atoms in the PT-NW. Meanwhile, K atoms are expelled from the lattice, probably in the form of $\text{KOH}(\text{aq})$. The continuous replacement of O atoms by N atoms and extrusion of K atoms would create defects and cause instability in the structure. At 873 K, formation of small crystallites on the NW surface was observed in Figure S7h in the Supporting Information. Above 973 K, the overall reaction and crystal growth rates accelerate. The high surface energy small crystallites coalesce and grow into large size ones. This can be attributed as an example of Ostwald ripening type of crystal growths.²⁵ The original NW not

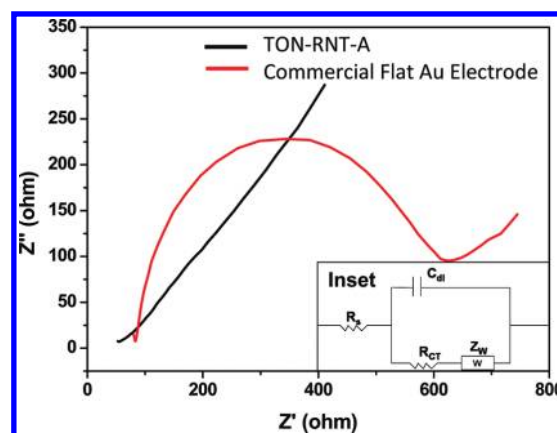


Figure 9. Nyquist diagrams of EIS analyses. TON-RNT-A/SPC and a commercial flat Au electrode were used as the working electrodes in a three-electrode system. Inset shows an equivalent circuit of the EIS analyses.

only serves as the reactant but also the template to sculpt the product's morphology. In Figure 8, the TEM studies of a TON sample grown at 973 K are shown. Formation of NRs is found in Figure 8a. One of the NRs is covered by crystallites with 70–80 nm in sizes (Figure 8a, b). Although in the images the NRs appear to be polycrystalline, the SAED pattern taken from the body of the NR, as shown in Figure 8c, suggests it is a single crystal. The HRTEM image of the squared area in Figure 8b, taken from the interface of the NR and a NP, does not display the presence of a boundary. The lattice spacings are 0.21 nm (Figure 8d). This is assigned to the distance between (020) planes of the cubic TiN_xO_y with the zone axis [001]. Other observation and characterization of the product TON-NR are listed in Table 1 and in the Supporting Information (Table S2 and Figure S7). The EA analyses showed that the N wt % in TON-NR and PT-NW-973–20 were much lower than those in TON-RNT-A and TON-RNT-B. It is interesting to note that the nitridation of PT-NW at 973 K produced TON-NR with a lower N concentration, whereas that at 1073 K generated TON-RNT-A and TON-RNT-B with higher N contents. The discrepancy can be rationalized by the difference of the reaction rates at these temperatures. It is reasonable that at 973 K, the rate was comparatively slower than the rate at 1073 K. As a consequence, the original NWs reacted slowly with NH_3 and converted gradually into the NRs with lower N contents and solid cores. In Figure 8, we also observe that the crystallite size in the NRs is 70–90 nm, much larger than the ones in TON-RNTs. It is evident that nitridation at 973 K caused small crystallites to recrystallize into large particles, probably through a slow Ostwald ripening process. Prolonged nitridation degraded the NRs into aggregates of particles (see Table S2 and Figure S7 in the Supporting Information). On the other hand, the nitridation on the NW surface was accelerated at 1073 K. When the crystallites grew on the NW surface, they consumed the NW skeleton rapidly. The process transformed the material into the observed RNT structures with higher N contents and empty cores. Moreover, as shown in Figures 4 and 6, the NH_3 flow rate affected the RNT morphology. For example, in a slower flow rate of 20 sccm, TON-RNT-A was produced. It had a single-crystal tube body and a rectangular tube cross-section. The observations suggest that under the low NH_3 flow rate condition, the nitridation process was not fast so that the as-formed oxynitride crystallites could align into the

Table 2. Summary of Variables Derived from EIS Analyses

	TON-RNT-A/SPC Electrode	Commercial Flat Au Electrode
R_s (Ω)	54	85
R_{CT} (Ω)	20	480
C_{dl} (F)	1.05×10^{-6}	2.40×10^{-6}
Z_w ($\Omega s^{1/2}$)	0.0008	0.0017
σ	0.055	0.055

ordered state gradually. On the other hand, in a higher flow rate of 50 sccm, TON-RNT-B was generated. It possessed a slightly less-ordered tube wall composed of particles and a round tube cross-section. On the basis of the observations, we propose that the reaction rate plays an important role affecting the final product morphologies.

Potential for Electrochemical Electrode Applications. The potential of the TiN_xO_y NTs for electrochemical applications was explored. To analyze their charge transfer properties, we conducted an EIS study for TON-RNT-A/SPC. Figure 9 shows its Nyquist diagram. The inset of Figure 9 displays the equivalent circuit and the components R_s , R_{CT} , C_{dl} , and Z_w , representing solution resistance, charge transfer resistance, double layer capacitance, and Warburg impedance, respectively. The fitted variables are listed in Table 2. TON-RNT-A/SPC shows a very low charge transfer resistance, 20 Ω . This is much lower than the value of the commercial flat Au electrode, 480 Ω . Clearly, the nitridation converted TON-RNT-A from an insulator to a conductor. To compare the charge transfer ability of TON-RNT-A/SPC with a bare SPC electrode, their CV data were shown in Figure S9 in the Supporting Information. For TON-RNT-A/SPC, the redox peak separation was about 100 mV, which was much narrower than the difference found for the SPC electrode, 500 mV. Moreover, TON-RNT-A/SPC showed an anodic current three times higher than that of the SPC electrode. The result suggests that TON-RNT-A can significantly enhance the charge transfer efficiency on the SPC electrode. CVs of ferricyanide redox reactions performed at varied scan rates are often used to estimate ESAs for electrodes by using the Randles–Sevcik equation $I_p = 2.69 \times 10^5 AD_o^{1/2} n^{3/2} C_o v^{1/2}$.²⁶ Here, I_p is the reduction peak current in mA, A is the electrode ESA in cm^2 , D_o is the diffusion coefficient of ferricyanide ($7.01 \times 10^{-6} cm^2/s$),²⁷ n is the number of electrons transferred in the reaction equation, C_o is the concentration of ferricyanide in M, and v is the scan rate in V/s. Ideally, this equation should be applied to electrodes with smooth surface and redox peaks separated at 59 mV. Although the TON-RNT-A/SPC was not an ideal case, we employed the equation for a qualitative estimation of its ESA. Figure 10 shows the CV diagrams obtained at varied scan rates. From the linear fitting of the currents of $K_3[Fe(CN)_6]$ on the electrode versus the square root of scan rates, the obtained slope could be employed to calculate the ESA of the electrode by assuming that the redox reaction of ferricyanide on TON-RNT-A/SPC was a quasi-reversible process. The inset of Figure 10 displays the fitted line from the CV data with a correlation coefficient $R = 0.9995$. The ESA of the composite electrode is calculated to be 0.32 cm^2 from the slope of the plot. This is a significant increase from the geometric area of the SPC electrode, 0.2 cm^2 . The results discussed above suggest that the TiN_xO_y nanostructures can be employed for electrochemical

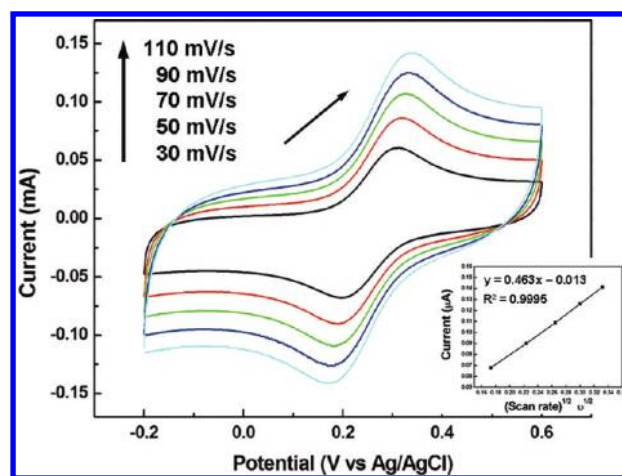


Figure 10. CVs of TON-RNT-A/SPC in $K_3[Fe(CN)_6](aq)$ (2 mM) and $KCl(aq)$ (1 M) at different scan rates. Inset shows responses of reduction peak currents to square root of scan rates of the electrode.

electrode applications. This is due to their large surface areas and low charge transfer resistances.

CONCLUSIONS

In this study, we synthesized PT-NWs by direct oxidation of titanium powders mixed with KF in water vapor at a high temperature. High-density NWs with several micrometers in length were obtained. The presence of KF was found to be crucial to the growths. Further nitridation of the PT-NWs at high temperatures in $NH_3(g)$ produced 1D TiN_xO_y nanostructures. These 1D nanostructures were characterized to be single crystalline cubic phase titanium oxynitride materials with preferred [200] orientations. We propose that the formation mechanism of the 1D TiN_xO_y nanostructures was via an Ostwald ripening type crystal growth process. In the process, nucleation and crystallization of the new solid state material converted the original PT-NWs into the nanostructures observed. In addition, the TON-RNTs were fabricated into an electrode which showed promising electrochemical behaviors. This suggests that the TON-RNTs may be employed as potential electrode materials for electrochemical applications in the future.

ASSOCIATED CONTENT

Supporting Information. Experimental setups, tables of summaries of reactions, lists of diffraction data, list of Ti and N contents, EDX results, SEM images, XRD patterns, TEM images, ED pattern, TGA data, XPS spectra, and CV data. This material is available free of charge via the Internet at <http://pubs.acs.org>.

AUTHOR INFORMATION

Corresponding Author

*E-mail: htchiu@faculty.nctu.edu.tw.

ACKNOWLEDGMENT

We thank the National Science Council, "Aim for the Top University Plan" of the National Chiao Tung University, and the Ministry of Education of Taiwan, the Republic of China for support. Also, we thank Prof. Teng-Ming Chen for experimental assistance.

■ REFERENCES

- (1) Chiu, H.-T.; Chuang, S.-H.; Lee, G.-H.; Peng, S.-M. *Adv. Mater.* **1998**, *10*, 1475.
- (2) Sirvio, E. H.; Sulonen, M.; Sundquist, H. *Thin Solid Films* **1982**, *96*, 93.
- (3) Latella, B. A.; Gan, B. K.; Davies, K. E.; McKenzie, D. R.; McCulloch, D. G. *Surf. Coat. Technol.* **2006**, *200*, 3605.
- (4) Song, X.; Gopireddy, D.; Takoudis, C. G. *Thin Solid Films* **2008**, *516*, 6330.
- (5) Kim, K. H.; Lee, S. H. *Thin Solid Films* **1996**, *283*, 165.
- (6) Choi, D.; Kumta, P. N. *J. Electrochem. Soc.* **2006**, *153*, A2298.
- (7) Furimsky, E. *Appl. Catal., A* **2003**, *240*, 1.
- (8) Jiang, Q. W.; Li, G. R.; Gao, X. P. *Chem. Commun.* **2009**, 6720.
- (9) Li, G. R.; Wang, F.; Jiang, Q. W.; Gao, X. P.; Shen, P. W. *Angew. Chem., Int. Ed.* **2010**, *49*, 3653.
- (10) Ostermann, D.; Jacobs, H.; Harbrecht, B. *Z. Anorg. Allg. Chem.* **1993**, *619*, 1277.
- (11) Nachiappan, A.; Andreas, H.; Jansen, M. *Z. Anorg. Allg. Chem.* **2003**, *629*, 939.
- (12) Zhang, Z.; Goodall, J. B. M.; Morgan, D. J.; Brown, S.; Clark, R. J. H.; Knowles, J. C.; Mordan, N. J.; Evans, J. R. G.; Carley, A. F.; Bowker, M.; Darr, J. A. J. *Eur. Ceram. Soc.* **2009**, *29*, 2343.
- (13) Chakrapani, V.; Thangala, J.; Sunkara, M. K. *Int. J. Hydrogen Energy* **2009**, *34*, 9050.
- (14) Zukalova, M.; Prochazka, J.; Bastl, Z.; Duchoslav, J.; Rubacek, L.; Havlicek, D.; Kavan, L. *Chem. Mater.* **2010**, *22*, 4045.
- (15) Jeon, S.; Kim, H.; Yong, K. *J. Vac. Sci. Technol., B* **2009**, *27*, 671.
- (16) Zhao, Y. M.; Hu, W. B.; Xia, Y. D.; Smith, E. F.; Zhu, Y. Q.; Dunnill, C. W.; Gregory, D. H. *J. Mater. Chem.* **2007**, *17*, 4436.
- (17) Joshi, U. A.; Chung, S. H.; Lee, J. S. *J. Solid State Chem.* **2005**, *178*, 755.
- (18) Cheung, K.; Yip, C.; Djuriscaroni, A.; cacute; Leung, Y.; Chan, W. *Adv. Funct. Mater.* **2007**, *17*, 555.
- (19) Ho, L. N.; Ishihara, T.; Ueshima, S.; Nishiguchi, H.; Takita, Y. *J. Colloid Interface Sci.* **2004**, *272*, 399–403.
- (20) NIST X-ray Photoelectron Spectroscopy Database 2007, <http://srdata.nist.gov/xps/Default.aspx>.
- (21) Ban, V. S. *J. Electrochem. Soc.* **1972**, *119*, 761–765.
- (22) Tsyganenko, A. A.; Pozdnyakov, D. V.; Filimonov, V. N. *J. Mol. Struct.* **1975**, *29*, 299.
- (23) Dwikusuma, F.; Kuech, T. F. *J. Appl. Phys.* **2003**, *94*, S656.
- (24) Kagami, S.; Onishi, T.; Tamaru, K. *J. Chem. Soc., Faraday Trans. I* **1984**, *80*, 29.
- (25) Mariadassou, G. D.; Shin, C. H.; Bugli, G. *J. Mol. Catal. A: Chem.* **1999**, *141*, 263.
- (26) Ostwald, W. *Lehrbuch der Allgemeinen Chemie*; W. Engelmann: Leipzig, Germany, 1887.
- (27) Bard, A. J.; Faulkner, L. *Electrochemical Methods: Fundamentals and Applications*; 2nd ed.; Wiley: New York, 2001.
- (28) Petrovic, S. *Chem. Educator* **2000**, *5*, 231.